Magnetic solitons and magnetic phase diagram of the hexagonal chiral crystal $CrNb_3S_6$ in oblique magnetic fields

Jun-ichiro Yonemura,[1] Yusuke Shimamoto,[1] Takanori Kida,[2] Daichi Yoshizawa,[2] Yusuke Kousaka,[3,4,5,6] Sadafumi Nishihara,[3,4] Francisco Jose Trindade Goncalves,[1,3] Jun Akimitsu,[3,4,5,6] Katsuya Inoue,[3,4,7] Masayuki Hagiwara,[2,3] and Yoshihiko Togawa[1,3]

[1]*Department of Physics and Electronics, Osaka Prefecture University, 1-2 Gakuencho, Sakai, Osaka 599-8570, Japan*
[2]*Center for Advanced High Magnetic Field Science, Graduate School of Science, Osaka University, Toyonaka, Osaka 560-0043, Japan*
[3]*Chirality Research Center, Hiroshima University, Higashi-Hiroshima, Hiroshima 739-8526, Japan*
[4]*Graduate School of Science, Hiroshima University, Higashi-Hiroshima, Hiroshima 739-8526, Japan*
[5]*Department of Physics and Mathematics, Aoyama Gakuin University, Sagamihara, Kanagawa 252-5258, Japan*
[6]*Graduate School of Science, Okayama University, Okayama 700-8530, Japan*
[7]*IAMR, Facility of Science, Hiroshima University, Higashi-Hiroshima, Hiroshima 739-8530, Japan*

We investigate the magnetic torque and magnetoresistance (MR) responses in oblique magnetic fields in micrometer-sized specimens of the hexagonal chiral magnetic crystal $CrNb_3S_6$. The results exhibit hysteresis over a wide range of applied field angles, while reversible behavior appears only when the magnetic field is closely aligned to the helical axis of the crystal. Stepwise changes of the magnetic torque and MR detected in the hysteresis region indicate the existence of chiral solitons in the oblique magnetic fields. A magnetic phase diagram is derived from the experimental results, and the stability of the chiral magnetic phases, such as the chiral soliton lattice and chiral conical phase, and the nature of the phase transition between them are discussed.

I. INTRODUCTION

A chiral magnetic order appears in a particular class of magnetic materials without rotoinversion symmetry. Namely, a chiral magnetic crystal is one of the promising materials for device applications in spin electronics because it exhibits many kinds of emergent physical properties due to the nonlinear, robust, topological, and tunable nature of the chiral magnetic order. Indeed, various material functions characteristic of the chiral magnetic order and materials are discussed in the literature [1–4]. Furthermore, because of the universality of the concept of chirality, chiral magnetism has attracted attention in many research areas, such as soft-matter physics [5,6], molecular chemistry [7,8], and nanophotonics [9,10].

The formation of the chiral magnetic order occurs as a consequence of the competition between the symmetric Heisenberg and antisymmetric Dzyaloshinskii-Moriya (DM) exchange interactions [11,12] in the presence or absence of an external magnetic field H. The types of chiral magnetic phases are categorized based on the symmetry of the chiral magnetic materials. Several examples of the chiral magnetic phases formed in a monoaxial chiral magnetic crystal are schematically drawn in Fig. 1.

A chiral helimagnetic order (CHM) appears at zero magnetic field, as illustrated in Fig. 1(a). The helical pitch $L(0)$ of the chiral twist array is determined by the ratio of two kinds of exchange interactions and does not necessarily match the unit size of the hosting crystalline lattice. Thus, the CHM corresponds to an incommensurate (IC) phase. The application of H induces different kinds of transformations from the CHM depending on the relative configuration between the directions of H and the helical axis.

When H is applied along the direction parallel to the helical axis ($H_\parallel$), the CHM transforms into a chiral conical phase, as drawn in Fig. 1(b). As the strength of $H_\parallel$ increases, the magnetic moments of the chiral conical phase tilt toward the helical axis, and thus, the helical pitch remains constant as $L(0)$. The chiral conical phase remains incommensurate during the continuous transformation into a commensurate (C) forced ferromagnetic (FM) state which is formed above the critical magnetic field in the $H_\parallel$ configuration ($H_c^\parallel$).

When H is applied in the direction perpendicular to the helical axis ($H_\perp$), another important chiral magnetic phase appears, that is, a nonlinear helicoidal superlattice called a chiral soliton lattice (CSL) [13–16]. The CHM which appears at zero field transforms into the CSL in the presence of $H_\perp$. As presented in Fig. 1(c), the CSL consists of chiral soliton kinks which periodically partition forced FM regions. The FM regions gradually expand in the CSL, and thus, the period $L(H)$ of the CSL grows with increasing field strength. The CSL eventually transforms into the forced FM state above the critical magnetic field in the $H_\perp$ configuration ($H_c^\perp$). The number of chiral solitons, corresponding to the winding number, is altered as a function of $H_\perp$ during the CSL formation [15,16]. Therefore, the process of the CSL formation corresponds to a different type of the IC-C phase transition. In other words, the nature of the phase transition for the CSL formation in $H_\perp$ should be different from that for the formation of the chiral conical phase in $H_\parallel$.

The stability of chiral solitons is an important factor when it comes to the control of the physical response of the chiral magnetic system. In this regard, the phase diagram of the chiral magnetic phases under the oblique magnetic fields is a matter of interest [17] but remains unclear. More precisely, numerical simulations [17] predicted the existence of two tricritical points among the CSL, chiral conical, and forced FM phases at tilted field angles of 88.5° and 81.5° from the ab plane in the magnetic phase diagram under the oblique magnetic fields (for details, see Sec. V). To test the validity of this theoretical prediction, the region where the chiral
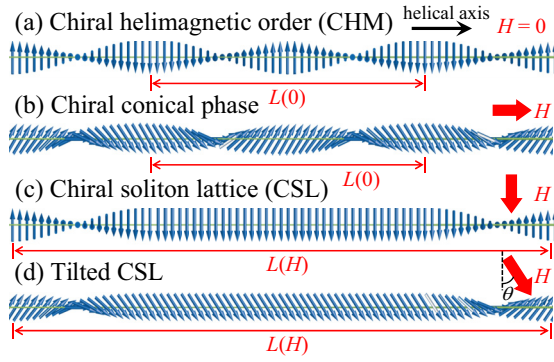
FIG. 1. Schematics of the chiral magnetic phases formed in a monoaxial chiral magnetic crystal. (a) Chiral helimagnetic order (CHM) at zero magnetic field. (b) Chiral conical phase in H applied parallel to the helical axis. (c) Chiral soliton lattice (CSL) in H perpendicular to the helical axis. (d) Tilted CSL under the oblique H. The pitch of the chiral conical phase remains $L(0)$, while the magnetic moments cant towards H. The period $L(H)$ of the CSL and tilted CSL phases changes as a function of H. The principal axis of the monoaxial crystal corresponds to the helical axis.

solitons survive in the oblique field phase diagram should be determined experimentally.

In this paper, we have investigated the magnetic states of micrometer-sized specimens of a hexagonal chiral magnetic crystal $CrNb_3S_6$ in fields applied at an oblique angle to the helical c axis. Specimens with reduced dimensions, e.g., in micrometer scale, are advantageous to examine the existence of the chiral solitons in the system [4]. Magnetoresistance (MR) measurements performed in micrometer-sized platelet specimens in the $H_\perp$ configuration [18] revealed that hysteresis and stepwise behavior of the MR signals become increasingly prominent with decreasing sample size. These features contrast with the continuous changes of the MR curves observed in the bulk crystals [19] and result from chiral solitons entering and being expelled from the system with a finite size. Indeed, the elaborate examinations using transmission electron microscopy directly demonstrated such a finite-size effect [18]. The visualization of chiral solitons during the H cycle in a crystalline grain with a fixed handedness (typically, as small as several micrometers or less) sandwiched by grains with the opposite handedness exhibited many plateaus of the CSL period as well as discretized changes of the soliton number. Soliton confinement in a finite-size system, as exemplified by micrometer-sized platelet specimens with edges and crystalline "chirality" grains with boundaries, is responsible for triggering a discretized (quantized) and hysteresis response of the physical properties. Such hysteresis and stepwise behavior in turn provide evidence of the existence of chiral solitons in the system subject to oblique fields. However, the signal intensity generated by changes in the number of chiral solitons is weak and requires sensitive measurements, particularly for measuring the magnetization.

In this study, magnetic torque measurements using a microcantilever were performed to directly evaluate the magnetization under the oblique fields. The magnetic torque, which is sensitive to a relative and small change in the magnetic moments, allowed us to identify the hysteresis region

of the magnetization and detect its discrete changes due to single-soliton entry and removal in the specimens with varying H. These results indicate the existence of chiral solitons in the system under oblique fields. When H is oriented nearly along the c axis, the magnetic torque becomes reversible and shows no hysteresis. Such behavior was also observed in the MR data of the micrometer-sized crystals under the oblique fields.

The results obtained by the complimentary magnetic torque and MR measurements in the micrometer-sized specimens reveal that the continuous phase transition due to the formation of the chiral conical phase is realized solely in the vicinity of the $H_\parallel$ configuration. This behavior is consistent with the existence of the numerically predicted first tricritical point at $88.5°$ [17]. On the other hand, as evidenced by the hysteresis and stepwise behavior of the signals, no indication of the second tricritical point at $81.5°$ [17] was obtained below the first tricritical point. Thus, it is concluded that the tilted CSL forms in a wide range of oblique H angles in the magnetic phase diagram.

This paper is organized as follows. In Sec. II, experimental methods, in particular, details of the magnetic torque measurement using a microcantilever, are described. Section III explains the magnetic torque data in the micrometer-sized $CrNb_3S_6$ crystals. Section IV provides the MR data. Section V provides the magnetic phase diagram and deals with the comparison of the experimental results with numerical results reported previously [17]. A summary is given in Sec. VI.

II. EXPERIMENTAL METHODS

The transition-metal dichalcogenide $CrNb_3S_6$ has a hexagonal crystalline structure belonging to the space group $P6_322$. The helical period $L(0)$ of the CHM is 48 nm below 100 K. Because of the in-plane magnetic anisotropy, the magnetic moments of the CHM and the CSL rotate within the ab plane normal to the helical c axis. Bulk single crystals of $CrNb_3S_6$ were grown using a chemical-vapor transport method, as described elsewhere [20]. The critical temperature T_c of the bulk crystal used in this study is 127 K. $H_c^\perp$ is 1.8 kOe, while $H_c^\parallel$ is 19.5 kOe. These values are consistent with those reported in the literature [16,18–26]. The value of $H_c^\perp$ is increased up to about 3 kOe due to the demagnetization effect depending on the specimen geometry as well as the configuration of the crystalline axis and H direction [4,18]. The micrometer-sized specimens were fabricated from this crystal, as described below.

A magnetic torque $\boldsymbol{\tau} \propto \boldsymbol{m} \times \boldsymbol{H}$ is induced in the crystal by application of a magnetic field $\boldsymbol{H}$, where $\boldsymbol{m}$ is the magnetic moment of the crystal. $CrNb_3S_6$ is a highly anisotropic helimagnetic crystal with a hard-axis anisotropy along the c axis [4]. At zero H, it has magnetic moments rotating within the ab plane and hence exhibits zero magnetization and no signal of the magnetic torque. When H is applied in the direction oblique to the ab plane, a magnetic torque is generated.

Figure 2 shows the experimental setup for detecting the magnetic torque using a microcantilever [Fig. 2(a)] combined with an electric circuit of a Wheatstone bridge [Fig. 2(b)] [27]. A micrometer-sized crystal was cut from the bulk crystal and set on the head of the microcantilever using a focused ion
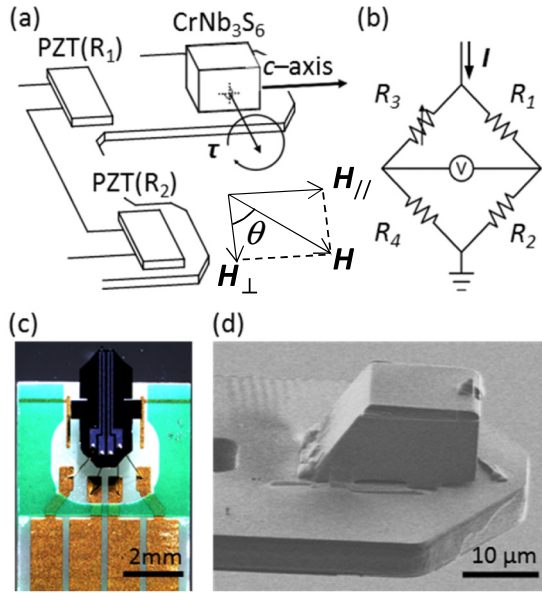
FIG. 2. (a) Schematics of the experimental setup of the magnetic torque measurement using a microcantilever. The longitudinal direction of the microcantilever is set to be along the c axis of the crystal. The external H, which is fixed to be along the vertical direction, has an angle θ to the ab plane. (b) Wheatstone bridge circuit for detection of a relative change of the piezoelectric signal in the PZT device R_1 induced by the magnetic torque. The PZT devices (monitor R_1 and reference R_2) located on the microcantilever are inserted into a cryostat, while the tunable R_3 and the other reference R_4 are set up to form the electric circuit outside the cryostat. (c) Optical micrograph of the microcantilever. (d) Scanning ion micrograph of the head of the microcantilever on which the micrometer-sized $CrNb_3S_6$ crystal is located. The size of the crystal is $13.4\,\mu m \times 12.0\,\mu m \times 17.6\,\mu m$ ($\parallel c$ axis). The magnetic moments of the crystal are calculated to be 5×10^{-7} emu at 10 K. The magnetic moments per soliton are estimated to be 1.4×10^{-9} emu. These values provide the sensitivity of the present magnetic torque measurements.

beam machine [Figs. 2(c) and 2(d)]. In the experiments, the external H was fixed to point in the vertical direction, while the cantilever with the specimen was rotated with respect to the vertical direction. The magnitude of the magnetic torque is altered depending on the angle θ between the ab plane and H.

For precise detection of the magnetic torque, it was converted into the electric signal of a piezoelectric device made of a lead zirconate titanate (PZT) compound located on the bottom of the cantilever. The voltage signal was tuned to zero in the Wheatstone bridge circuit to provide a reference point for the torque measurement. For example, the tuning was performed at zero H. Then, the relative change in the voltage signal was measured as a function of H at a fixed θ using a current source and a nanovoltmeter. Thus, the measured signal represents a relative change in m and reflects the structure of the chiral magnetic order formed in the crystal.

As presented in the following section, the magnetic torque signals associated with the transformation of the chiral magnetic structures were successfully detected at H around or less than 1 T in the experiments. Using the volume of the specimen examined and the saturation magnetization

reported at 10 K, the estimated total magnetic moment is 5×10^{-10} A m^2 (5×10^{-7} emu). The magnetic moment for a single soliton is 1.4×10^{-12} A m^2 (1.4×10^{-9} emu), the detection of which is beyond the typical sensitivity of commercial magnetometers using a superconducting quantum interference device [25,26]. In the present technique, such a small value of magnetic moment generates a stepwise change of the magnetic torque signal of about 10^{-8} N m at H less than 1 T. In this regime of small magnetic fields, the magnetic torque of a single soliton was successfully measured, and the sensitivity of this method is evaluated to be of the order of 10^{-9} emu. This sensitivity for the magnetic moment has also been achieved in previous studies carried out at large H, typically larger than 10 T [27–30].

The MR curves were measured with the standard four-terminal ac resistance measurement in micrometer-sized lamella crystals of $CrNb_3S_6$. A typical dimension of the platelet specimens is 10 $\mu m \times$ 500 nm (within the ab plane) $\times$ 10 μm (along the c axis). H was applied in the direction normal to the largest plane of the specimens during the MR measurement. Thus, $H_c^{\perp}$ becomes 3010 Oe in the specimen presented in this paper. Details of the MR measurement procedure can be found elsewhere [18].

III. MAGNETIC TORQUE MEASUREMENTS

Figure 3(a) shows a typical magnetic torque curve of the micrometer-sized crystal presented in Fig. 2(d). The data were taken as a function of H at a fixed θ of 56° at 10 K. Here, θ is defined as schematically drawn in Figs. 1(d) and 2(a). A monotonic increase in the signal was observed with increasing H, and clear hysteresis behavior followed by a sudden reduction of the signal intensity was found with decreasing H.

In order to identify the hysteresis region more effectively, the magnetic torque signal of the H increase process was subtracted from that of the H decrease process. As exemplified in Fig. 3(b), it is clear that the hysteresis becomes negligibly small at small and large H regions. Additionally, the sharp jump in the magnetic torque signal can be easily identified. Here, three characteristic points are defined as $H_{\text{hys−open}}$, H_{jump}, and $H_{\text{hys−close}}$ in the magnetic torque curve, as indicated in Fig. 3. The decomposed value $H_{\text{hys−close}} \cos\theta$ at 56° was found to be close to but smaller than $H_c^{\perp}$ (2430 Oe) of this crystal.

The downward convex change in the magnetic torque curve was observed below $H_{\text{hys−close}}$ and H_{jump} in the H increase and decrease processes, respectively. Such behavior also appears in the magnetization curve in the $H_{\perp}$ configuration [19–22] and is known to be characteristic of the CSL formation, where the soliton density plays a role as the order parameter of the IC-C phase transition [15,31–33]. In other words, it originates from the process of how chiral solitons change during the CSL formation and indicates the existence of chiral solitons in the magnetic structure. Therefore, it can be concluded that the CSL forms even at $\theta = 56°$. Due to the presence of tilted fields, a deformed or tilted CSL phase is expected, as illustrated in Fig. 1(d). Then, the next question to be addressed is whether chiral solitons survive at higher values of θ.

Above $H_{\text{hys−close}}$, the linear dependence of the magnetic torque is found in Fig. 3(a). This result appears to suggest that
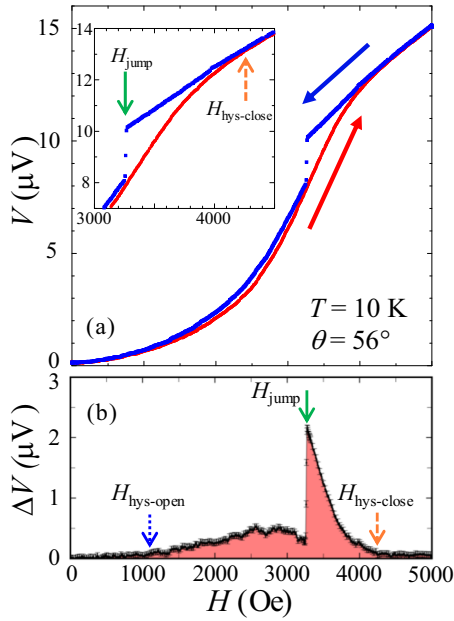
FIG. 3. (a) Magnetic torque curve of the micrometer-sized $CrNb_3S_6$ crystal obtained at a fixed θ of $56°$ at 10 K. The monitor current flowing in the Wheatstone bridge is 100 μA in all magnetic torque measurements performed in this study. The H sweep directions are given by solid arrows. The inset shows a zoomed-in view of the hysteresis region, where H_{jump} and $H_{hys-close}$ are indicated by solid and dashed arrows, respectively. (b) The hysteresis region identified by the subtraction of the data in the H increase process from that in the H decrease process. $H_{hys-open}$ (1080 Oe) is indicated by a dotted arrow in addition to H_{jump} (3270 Oe) and $H_{hys-close}$ (4230 Oe), with error bars of 50 nV.

m is collinear in a particular direction and the signal is simply proportional to the strength of H just after the forced FM state is formed. However, to obtain the magnetic torque signal in the forced FM state, a discrepancy is required between the m and H directions. Indeed, we will see below that there is a saturation and reduction of the magnetic torque signal with further increasing H in the forced FM state.

A set of the magnetic torque data was measured up to 20 kOe at various values of θ, as shown in Fig. 4. In Figs. 4(a) to 4(d), the magnetic torque curves show qualitatively the same (downward convex) behavior below $H_{hys-close}$. The saturation and reduction (or such a tendency) of the signal are observed above $H_{hys-close}$, as expected in the forced FM state.

To see quantitatively how the magnetic torque changes, the magnitude of the signal at $H_{hys-close}$, corresponding to a change in the signal from 0 Oe, as indicated by the orange bars in Fig. 4, is plotted as a function of θ in Fig. 5. The magnetic torque signal tends toward zero in the limit of $\theta = 0°$ ($H_\perp$ configuration), which is consistent with the expectation described above. With increasing θ, the signal becomes larger and larger but starts to decrease at around $80°$. It drops sharply to zero as θ approaches $90°$. In the experiments, the angle at which the magnitude of the signal was smallest was determined as $90°$ ($H_\parallel$ configuration). With elevating θ over $90°$, the signal changes its sign, and its magnitude increases again in the opposite direction. This change in sign of the magnetic torque signal is clearly seen, e.g., at $100°$, as shown in Fig. 4(f).
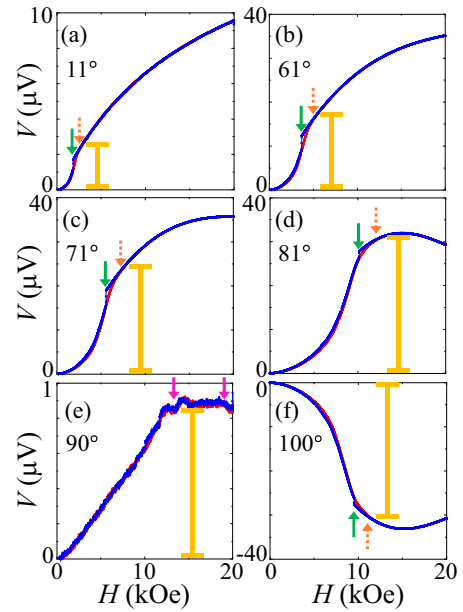

FIG. 4. Angular dependence of the magnetic torque curve at 10 K. H_{jump} and $H_{hys-close}$ are indicated by solid and dashed arrows in (a) to (d) and (f), respectively. The field region where the signal is saturated is indicated by solid arrows in (e). The sign of the signal is reversed above $\theta = 90°$, as seen in (f). The change in the signal from 0 Oe to $H_{hys-close}$ or to the saturated point is provided by the vertical orange bar in each panel.

The magnetic torque curve at $\theta = 90°$ shown in Fig. 4(e) is different from those obtained at other values of θ. The downward convex behavior of the signal is barely found. The signal becomes constant for a certain width of H and decreases at large H. The point where the signal decreases, as indicated by the vertical arrow in Fig. 4(e), shows good agreement with the value for $H_c^\parallel$. Importantly, the hysteresis disappears completely at $90°$.

Figure 6 shows the hysteresis region examined at various values of θ. Clearly, the field positions corresponding to $H_{hys-open}$, H_{jump}, and $H_{hys-close}$ vary significantly with θ. Moreover, it is found that the hysteresis becomes negligibly small between $89°$ and $91°$. The hysteresis disappears in the
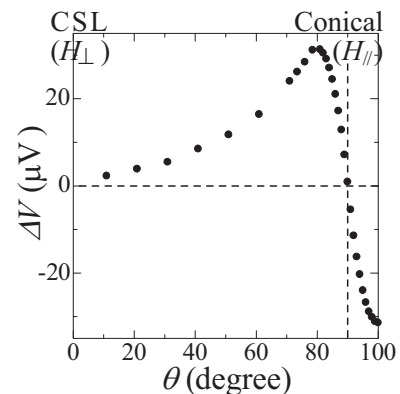

FIG. 5. The change in the magnetic torque between 0 Oe and $H_{hys-close}$ as a function of the angle.
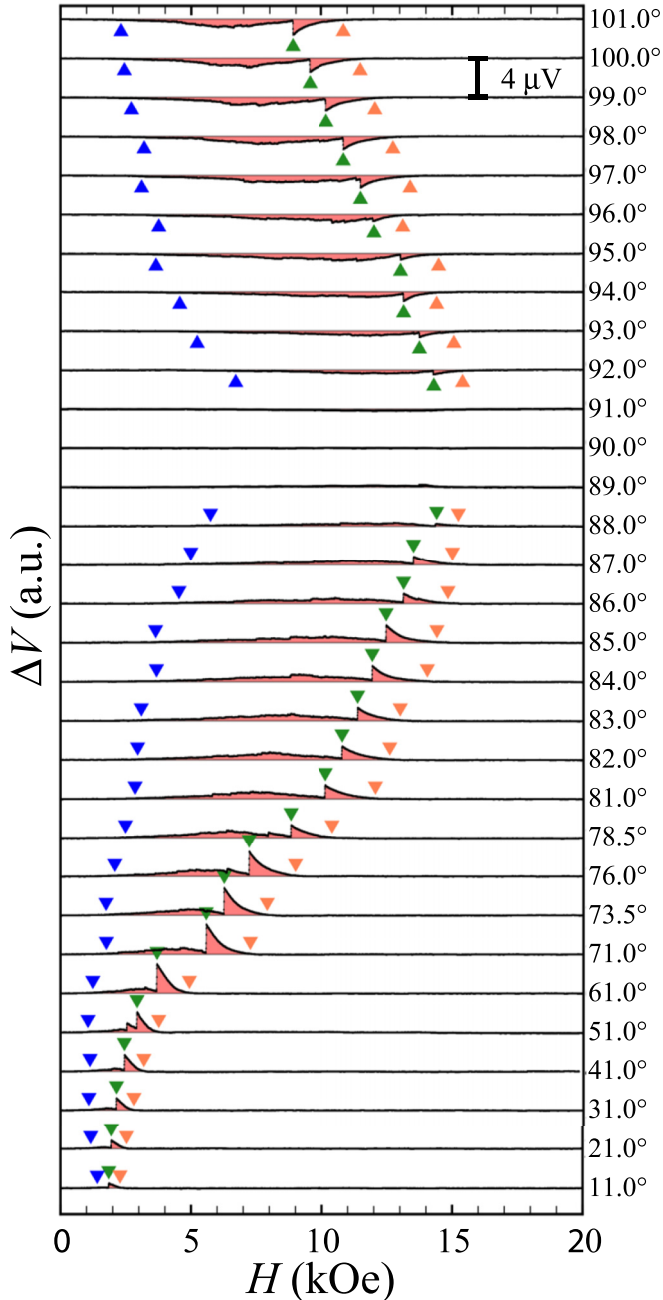
FIG. 6. The hysteresis region of the magnetic torque as a function of H at various angles. The data are shifted by 4 μV. $H_{\text{hys-open}}$, H_{jump}, and $H_{\text{hys-close}}$ are indicated by arrow heads from left to right, respectively.

FIG. 7. (a) Magnetic torque curve at $\theta = 87.5°$ at 10 K. Stepwise changes are observed in the hysteresis region, as indicated by horizontal bars in (b) to (e). The magnitude of the step is (b) 50 nV at 6.28 kOe, (c) 80 nV at 8.54 kOe, (d) 150 nV at 10.03 kOe, and (e) 100 nV at 11.04 kOe.

vicinity of the $H_\parallel$ configuration, where the chiral conical phase forms.

Figure 7 presents the magnetic torque curve at $\theta = 87.5°$, which is close to the region where the chiral conical phase appears. In addition to the characteristic behavior already pointed out above, including the large jump in the signal at 13.3 kOe, several stepwise changes in the signal were observed in the hysteresis region with decreasing H. The magnitude of the steps ranges from 50 to 150 nV. The specimen examined here has about 360 chiral solitons at $H = 0$, which is estimated
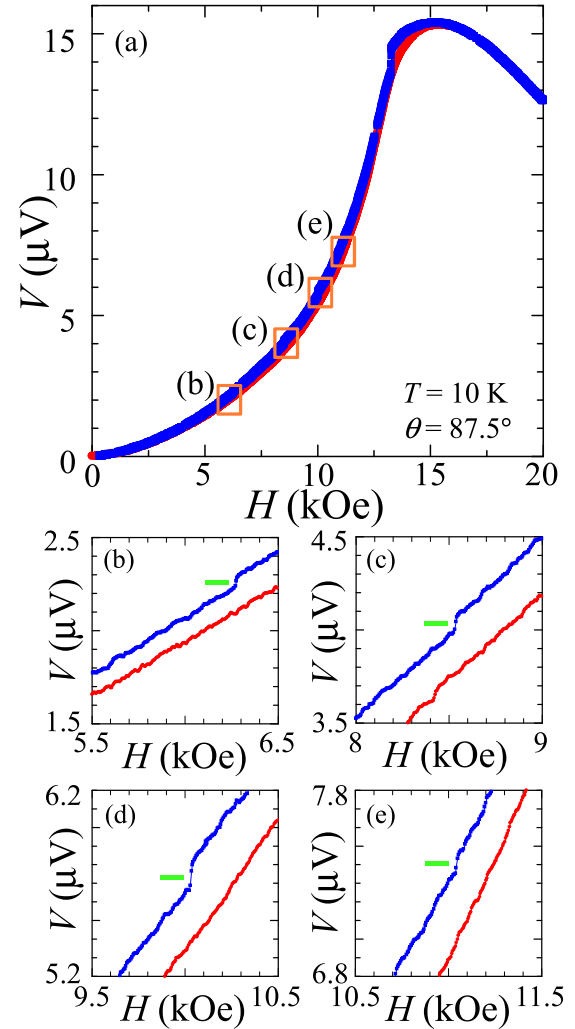
by dividing the specimen length along the c axis by the helical period $L(0)$ of 48 nm at $H = 0$ at 10 K. A rough estimation gives a magnetic torque signal of about 40 nV per soliton, which is on the same order of magnitude as the stepwise signals observed in Figs. 7(b) to 7(e). Thus, it is likely that single-soliton penetration was successfully detected in the present magnetic torque measurements. Similar stepwise changes in the magnetic torque signal were also observed at lower tilted angles.

Based on the experimental results obtained in the magnetic torque measurements, we can conclude that the hysteresis and stepwise changes in the magnetic torque are ascribed to the penetration or removal of the chiral solitons in the system, indicating the existence of chiral solitons in the magnetic structure in oblique fields, even at θ values as large as $87.5°$. Namely, the tilted CSL forms in most regions of the magnetic phase diagram under the oblique magnetic fields, while the chiral conical phase survives only in close vicinity to the $H_\parallel$ configuration.
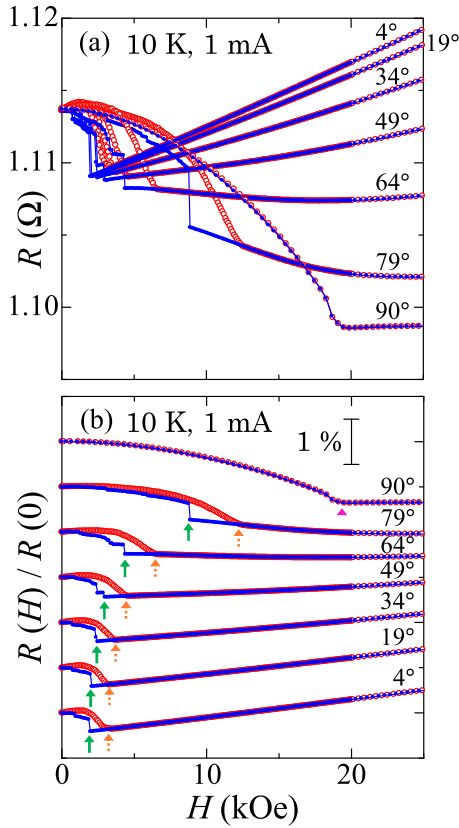
FIG. 8. Angular dependence of the MR of the micrometer-sized CrNb$_3$S$_6$ crystal. The raw MR data taken at various values of θ are given in (a), while the MR curves normalized by $R(0)$ of 1.1137 Ω are shifted vertically for clarity in (b). H_{jump} and $H_{\text{hys-close}}$ are indicated by solid and dotted arrows, respectively. $H_c^{\parallel}$ is given by the arrow head.
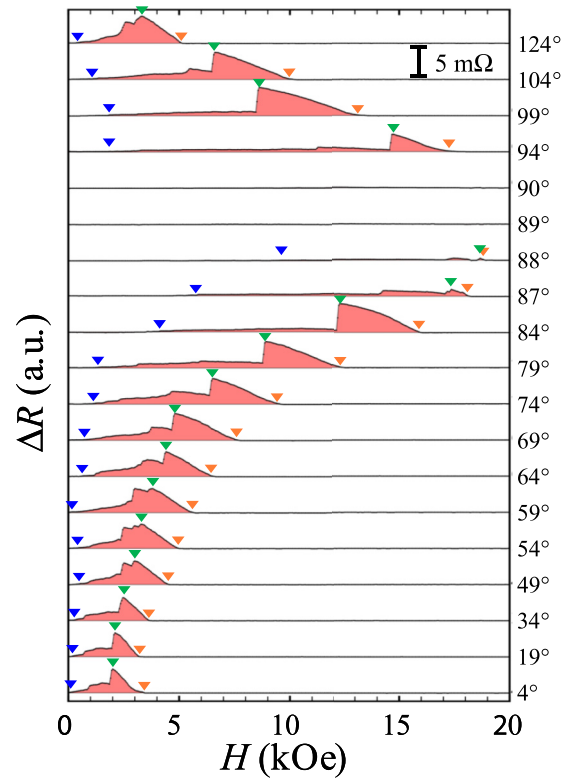

FIG. 9. The hysteresis region of the MR data at various angles. From low to high fields, the arrow heads indicate the positions of $H_{\text{hys-open}}$, H_{jump}, and $H_{\text{hys-close}}$.

IV. MAGNETORESISTANCE MEASUREMENTS

The angular dependence of the MR data was investigated to find the correlation between the magnetization examined by the magnetic torque measurements and electric transport properties under the oblique magnetic fields. In the $H_{\perp}$ configuration, previous studies clarified that the magnitude of the MR correlates well with the soliton density of the CSL [18,19]. Furthermore, the main advantage of the MR data is that they allow us to access the magnetic properties in the vicinity of both 0° and 90°. As described in the following paragraphs, the results have many of the same properties as those observed in the magnetic torque measurements given in Sec. III.

Figure 8 shows the MR curves at various values of θ, obtained at 10 K in the micrometer-sized CrNb$_3$S$_6$ crystal. Characteristic features of the data include a gradual decrease in the MR signal in the H increase process and a supersaturated behavior followed by a large jump in the MR in the H decrease process, except at around 90°. This behavior is consistent with that observed in the $H_{\perp}$ configuration [18]. Several plateaus of the MR signal are found in the H decrease process, for example, as seen at 49° and 64°. The origin of these discretized features are ascribed to the soliton confinement, as clarified in the $H_{\perp}$ configuration [18], and provide evidence of the

existence of chiral solitons under oblique magnetic fields. In the continuous MR curve obtained at $\theta = 90°$, a kink structure is found at 19.5 kOe, marked by an arrow head, which corresponds to $H_c^{\parallel}$ since the value is consistent with that for the bulk crystal [22].

Figure 9 shows the shift of the hysteresis region of the MR data toward large H with increasing θ, which is calculated in the same way as that for the magnetic torque curves. The hysteresis is hardly visible at 89° and 90°. Figure 10 shows the MR data at $\theta = 87°$. The stepwise changes in the MR signal are found in the hysteresis region and observed in a similar manner in a wide range of the oblique H angles below 87°. These observations are in good agreement with the magnetic torque data presented in Figs. 6 and 7.

V. DISCUSSION

To summarize the results of experimental observations, a magnetic phase diagram is constructed based on the MR and magnetic torque data, as shown in Fig. 11. The data for the H increase process is shown mainly in Fig. 11(a), while that for the H decrease process is shown in Fig. 11(b).

To identify the reversible region where the pure chiral conical phase exists, the MR and magnetic torque data at 89° and 90° as well as $H_{\text{hys-open}}$ for the MR are now discussed. Curves at both 89° and 90° show no hysteresis during the H cycle, as shown in Figs. 6 and 9. The values of $H_c^{\parallel}$ are determined at 89° and 90° in the MR curves, as partly shown in Fig. 8. $H_{\text{hys-open}}$ for the MR provides the boundary
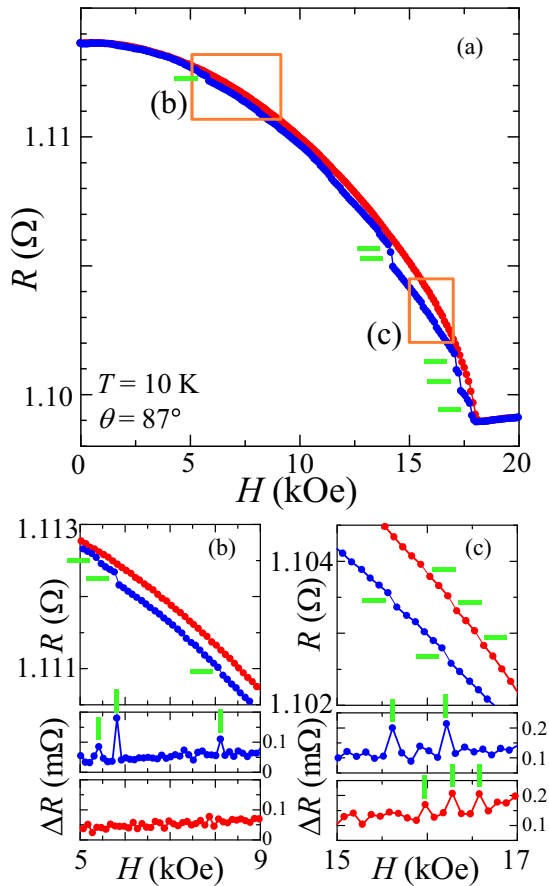
FIG. 10. The hysteresis behavior and stepwise changes of the MR data at $\theta = 87°$. Several large steps are visible, as indicated by horizontal bars in (a). The small steps, identified by the peak of the differential values ΔR between neighboring data points, are indicated by horizontal and vertical bars in (b) and (c).

FIG. 11. Magnetic phase diagram of the micrometer-sized CrNb$_3$S$_6$ crystal under oblique magnetic fields at 10 K. (a) Phase transition from IC chiral magnetic phases to the C forced FM phase in the H increase process. (b) Phase transition from C to IC phases in the H decrease process. Both axes are normalized with respect to the corresponding critical fields. The MR and magnetic torque data from $0°$ to $90°$ are given by solid and open symbols, respectively. $H_{\text{hys-open}}$ (blue), H_{jump} (green), and $H_{\text{hys-close}}$ (orange) are indicated by triangles, squares, and circles, respectively. $H_c^{\parallel}$ in the vicinity of the $H_{\parallel}$ configuration, which is determined in the MR data, is given by solid purple circles. The dashed black line serves as a guide for the eye to see the boundary between the chiral magnetic and forced FM phases. The dotted radial lines indicate the angle θ for the MR data. The locations of TC1 and TC2 predicted by numerical calculations are given on the $H_{\text{hys-close}}$ boundary line.

line between the reversible and hysteresis regions in the low-$H_{\perp}$ and -$H_{\parallel}$ region. An interpolation between these points determines the reversible region, shown in light blue. It is clearly seen that the chiral conical phase appears only in the vicinity of the $H_{\parallel}$ configuration.

On the other hand, the tilted CSL shows a change in the topological number of the chiral solitons, manifested by the hysteresis and stepwise behavior of the signal. $H_{\text{hys-close}}$ and H_{jump} are plotted separately in Figs. 11(a) and 11(b). Clearly, the nature of the phase transition from the IC to C phase is different from that from the C to IC phase. Upon increasing the strength of H at a fixed angle, the chiral solitons survive up to the $H_{\text{hys-close}}$ boundary line. In the MR data, the $H_{\text{hys-close}}$ line is smoothly connected to the $H_c^{\parallel}$ line at an angle between $88°$ and $89°$. Upon reducing the strength of H, the forced FM state is supersaturated down to the H_{jump} boundary line. The transient area between the H_{jump} and $H_{\text{hys-close}}$ lines for the supersaturated FM state is found in a wide range of the oblique H angles in the H decrease process. The slight deviation of the boundary lines between the MR and magnetic torque data may be ascribed to the difference in the shape of the specimens investigated. Also, the coupling of conduction electrons with the chiral magnetic phases probed by the MR may reflect the different physical aspect examined by the magnetic torque.
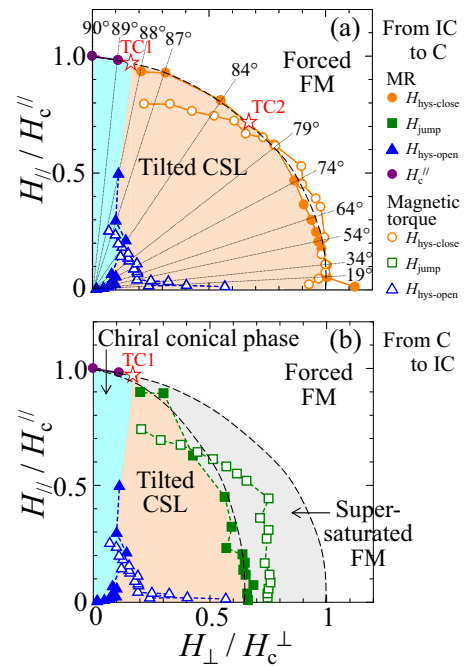
The nature of the phase transition between the different chiral topological phases, i.e., the CSL and chiral conical phases, is not fully understood. This subject was recently discussed by Laliena *et al.* [17]. Numerical calculations in an infinite system showed that the phase transition from the (IC) CSL or chiral conical phase to the (C) forced FM state should be continuous in the H configuration almost parallel to $H_{\perp}$ or $H_{\parallel}$, respectively. However, in the intermediate region with the oblique magnetic fields, the phase transition is discontinuous, and thus, the IC and C phases coexist around the transition line. By using material parameters of the CrNb$_3$S$_6$ crystal, the first and second tricritical points (TC1 and TC2) were estimated to be $(H_{\perp}, H_{\parallel}) = (0.59, 22.2)$ and $(1.86, 12.49)$ kOe, giving critical angles of $88.5°$ and $81.5°$, respectively.

The phenomenon associated with TC1 is expected to appear in a very narrow regime of the magnetic phase diagram. In the present experiments, the continuous phase transition was observed in the vicinity of the $H_{\parallel}$ configuration, and a small inclination of H from the helical c axis by a few degrees induced hysteresis in the magnetic torque and MR signals. In this respect, good agreement was found between

the experimental data and the numerical simulation [17], as indicated in Figs. 11(a) and 11(b). In other words, the formation of the chiral conical phase becomes robust and stable once the strict experimental condition for the continuous phase transition above TC1 is satisfied.

As for the existence of TC2, it is not clear whether a sign of this phenomenon is detected. The hysteresis region of the phase transition is found to appear below TC1 and expands down to the vicinity of the $H_\perp$ configuration, which coincides with the hysteresis behavior of the magnetization observed even at the $H_\perp$ configuration in bulk crystals [21–23,25,26]. The absence of TC2 in the experimental data may shed light on unidentified aspects of the robust formation of the chiral solitons in the system and require further theoretical considerations.

It is noted that, in the standard theoretical models, the nature of the phase transition is ideally discussed in the system in the thermodynamic limit where a large number of elements are involved with keeping the density constant. In this respect, in the case of the CrNb$_3$S$_6$ crystal, the length along the helical c axis of the available chiral magnetic crystals is typically several hundred micrometers, while the period of the chiral solitons is 48 nm. Thus, only several thousand solitons exist at $H = 0$ in the crystal. The limitation of the initial number of solitons involved in the phase transition in real materials may alter the nature of the phase transition, particularly in terms of the existence of hysteresis. There should be a nontrivial physical mechanism behind the phenomena observed. A microscopic understanding of the formation process of the chiral magnetic phases including the system size dependence is particularly required.

The existence of the chiral conical phase has great influence on the stabilization of other chiral magnetic phases. For example, in cubic chiral magnetic materials, where a chiral magnetic vortex called a magnetic skyrmion [34–37] can appear, the chiral conical phase coexists with a magnetic skyrmion or the CSL due to the first-order nature of the phase transition [38]. The internal structure between the chiral conical phase and other chiral phases, which has been discussed mainly from theoretical viewpoints [39], is also a nontrivial issue to be clarified. Furthermore, the chiral surface structure also contributes to the formation process and the stabilization of chiral magnetic vortices [39–42].

The monoaxial chiral crystals investigated in this study can provide a simpler model for the description of the magnetic phase diagram, where the CSL and the chiral conical phase compete with each other, than that for the topological counterparts realized in the cubic chiral crystals. In this connection, we believe that the present study provides important experimental evidence required to advance the understanding of how chiral magnetic phases can survive in the competition among themselves and the way to extract the

functionality arising from the stability of the chiral topological phases, which is unique to the chiral magnetic materials.

VI. SUMMARY

In this paper, we have investigated the magnetic torque and MR properties in terms of the formation of the chiral conical phase and chiral soliton twists in micrometer-sized crystals of the hexagonal chiral magnet CrNb$_3$S$_6$. Particularly, the existence and stability of the chiral solitons were examined under oblique magnetic fields.

Previous experiments [4,18,19] found that the penetration and removal of chiral solitons in the system induce hysteresis and stepwise behavior of the MR signal in the $H_\perp$ configuration in micrometer-sized specimens. As seen in Figs. 3 to 10, hysteresis behavior and stepwise changes were observed in both magnetic torque and MR data, indicating the existence of the chiral solitons in a wide range of oblique H angles irrespective of the slightly different geometries of specimens. Thus, it is found that the magnetic torque measurements using the microcantilever, which reflect the relative change of the magnetic moments, are useful for detecting the chiral solitons existing in the system subject to oblique magnetic fields. In particular, this method provides good sensitivity to directly detect discretized changes of the magnetic moments due to the penetration or removal of a single soliton.

We found that a pure chiral conical phase appears only in the vicinity of $H_\parallel$ of the magnetic phase diagram, while tilted and pure CSL structures stabilize over almost the whole range of oblique fields in the phase diagram. The stability of the chiral magnetic phases is an important and nontrivial subject that must be understood in order to utilize the various physical properties and functionality which the chiral magnetic phases exhibit [1–4]. From technological viewpoints, the stability of the chiral solitons observed in a wide range of the oblique H angles is in favor of device applications where the countable or topological nature of solitons is utilized as discretized or multivalued output signals [18,25,26,40,43,44].

[1] N. S. Kiselev, A. N. Bogdanov, R. Schäfer, and U. K. Rößler, J. Phys. D **44**, 392001 (2011).

[2] A. Fert, V. Cros, and J. Sampaio, Nat. Nanotechnol. **8**, 152 (2013).

[3] J. Kishine and A. S. Ovchinnikov, Solid State Phys. **66**, 1 (2015).

[4] Y. Togawa, Y. Kousaka, K. Inoue, and J. Kishine, J. Phys. Soc. Jpn. **85**, 112001 (2016).

[5] F. Lonberg and R. B. Meyer, Phys. Rev. Lett. **55**, 718 (1985).

[6] J.-i. Fukuda and S. Žumer, Phys. Rev. Lett. **104**, 017801 (2010); J. Fukuda and S. Žumer, Nat. Commun. **2**, 246 (2011).

[7] K. Inoue, H. Imai, P. S. Ghalsasi, K. Kikuchi, M. Ohba, H. Ōkawa, and J. V. Yakhmi, Angew. Chem., Int. Ed. **40**, 4242 (2001).

[8] K. Inoue, K. Kikuchi, M. Ohba, and H. Ōkawa, Angew. Chem., Int. Ed. **115**, 4958 (2003).

[9] I. Proskurin, A. S. Ovchinnikov, P. Nosov, and J. Kishine, New J. Phys. **19**, 063021 (2017).

[10] H. Fujita and M. Sato, Phys. Rev. B **95**, 054421 (2017).

[11] I. E. Dzyaloshinskii, J. Phys. Chem. Solids **4**, 241 (1958).

[12] T. Moriya, Phys. Rev. **120**, 91 (1960).

[13] I. E. Dzyaloshinskii, Zh. Eksp. Teor. Fiz. **46**, 1420 (1964) [Sov. Phys. JETP **19**, 960 (1964)].

[14] I. E. Dzyaloshinskii, Zh. Eksp. Teor. Fiz. **47**, 336 (1965) [Sov. Phys. JETP **20**, 223 (1965)].

[15] I. E. Dzyaloshinskii, Zh. Eksp. Teor. Fiz. **47**, 992 (1964) [Sov. Phys. JETP **20**, 665 (1965)].

[16] Y. Togawa, T. Koyama, K. Takayanagi, S. Mori, Y. Kousaka, J. Akimitsu, S. Nishihara, K. Inoue, A. S. Ovchinnikov, and J. Kishine, Phys. Rev. Lett. **108**, 107202 (2012).

[17] V. Laliena, J. Campo, J.-i. Kishine, A. S. Ovchinnikov, Y. Togawa, Y. Kousaka, and K. Inoue, Phys. Rev. B **93**, 134424 (2016).

[18] Y. Togawa, T. Koyama, Y. Nishimori, Y. Matsumoto, S. McVitie, D. McGrouther, R. L. Stamps, Y. Kousaka, J. Akimitsu, S. Nishihara, K. Inoue, I. G. Bostrem, V. E. Sinitsyn, A. S. Ovchinnikov, and J. Kishine, Phys. Rev. B **92**, 220412 (2015).

[19] Y. Togawa, Y. Kousaka, S. Nishihara, K. Inoue, J. Akimitsu, A. S. Ovchinnikov, and J. Kishine, Phys. Rev. Lett. **111**, 197204 (2013).

[20] Y. Kousaka, Y. Nakao, J. Kishine, M. Akita, K. Inoue, and J. Akimitsu, Nucl. Instrum. Methods Phys. Res., Sect. A **600**, 250 (2009).

[21] T. Moriya and T. Miyadai, Solid State Commun. **42**, 209 (1982).

[22] T. Miyadai, K. Kikuchi, H. Kondo, S. Sakka, M. Arai, and Y. Ishikawa, J. Phys. Soc. Jpn. **52**, 1394 (1983).

[23] N. J. Ghimire, M. A. McGuire, D. S. Parker, B. Sipos, S. Tang, J.-Q. Yan, B. C. Sales, and D. Mandrus, Phys. Rev. B **87**, 104403 (2013).

[24] B. J. Chapman, A. C. Bornstein, N. J. Ghimire, D. Mandrus, and M. Lee, Appl. Phys. Lett. **105**, 072405 (2014).

[25] K. Tsuruta, M. Mito, Y. Kousaka, J. Akimitsu, J. Kishine, Y. Togawa, H. Ohsumi, and K. Inoue, J. Phys. Soc. Jpn. **85**, 013707 (2016).

[26] K. Tsuruta, M. Mito, Y. Kousaka, J. Akimitsu, J. Kishine, Y. Togawa, and K. Inoue, J. Appl. Phys. **120**, 143901 (2016).

[27] E. Ohmichi and T. Osada, Rev. Sci. Instrum. **73**, 3022 (2002).

[28] C. Bergemann, Ph.D. thesis, University of Cambridge, 1999.

[29] C. Lupien, B. Ellman, P. Grutter, and L. Taillefer, Appl. Phys. Lett. **74**, 451 (1999).

[30] C. Rossel, P. Bauer, D. Zech, J. Hofer, M. Willemin, and H. Keller, J. Appl. Phys. **79**, 8166 (1996).

[31] P.-G. de Gennes, Solid State Commun. **6**, 163 (1968).

[32] Y. A. Izyumov, Sov. Phys. Usp. **27**, 845 (1984).

[33] J. Kishine, K. Inoue, and Y. Yoshida, Prog. Theor. Phys. Suppl. **159**, 82 (2005).

[34] A. N. Bogdanov and D. A. Yablonskii, Zh. Eksp. Teor. Fiz. **95**, 178 (1989) [Sov. Phys. JETP **68**, 101 (1989)].

[35] A. Bogdanov and A. Hubert, J. Magn. Magn. Mater. **138**, 255 (1994); **195**, 182 (1999).

[36] A. N. Bogdanov, U. K. Rößler, M. Wolf, and K.-H. Muller, Phys. Rev. B **66**, 214410 (2002).

[37] X. Z. Yu, Y. Onose, N. Kanazawa, J. H. Park, J. H. Han, Y. Matsui, N. Nagaosa, and Y. Tokura, Nature (London) **465**, 901 (2010).

[38] A. O. Leonov, Y. Togawa, T. L. Monchesky, A. N. Bogdanov, J. Kishine, Y. Kousaka, M. Miyagawa, T. Koyama, J. Akimitsu, Ts. Koyama, K. Harada, S. Mori, D. McGrouther, R. Lamb, M. Krajnak, S. McVitie, R. L. Stamps, and K. Inoue, Phys. Rev. Lett. **117**, 087202 (2016).

[39] D. McGrouther, R. J. Lamb, M. Krajnak, S. McFadzean, S. McVitie, R. L. Stamps, A. O. Leonov, A. N. Bogdanov, and Y. Togawa, New J. Phys. **18**, 095004 (2016).

[40] M. N. Wilson, E. A. Karhu, D. P. Lake, A. S. Quigley, S. Meynell, A. N. Bogdanov, H. Fritzsche, U. K. Rößler, and T. L. Monchesky, Phys. Rev. B **88**, 214420 (2013).

[41] F. N. Rybakov, A. B. Borisov, and A. N. Bogdanov, Phys. Rev. B **87**, 094424 (2013); F. N. Rybakov, A. B. Borisov, S. Blugel, and N. S. Kiselev, Phys. Rev. Lett. **115**, 117201 (2015).

[42] S. A. Meynell, M. N. Wilson, H. Fritzsche, A. N. Bogdanov, and T. L. Monchesky, Phys. Rev. B **90**, 014406 (2014).

[43] F. J. T. Goncalves, T. Sogo, Y. Shimamoto, Y. Kousaka, J. Akimitsu, S. Nishihara, K. Inoue, D. Yoshizawa, M. Hagiwara, M. Mito, R. L. Stamps, I. G. Bostrem, V. E. Sinitsyn, A. S. Ovchinnikov, J. Kishine, and Y. Togawa, Phys. Rev. B **95**, 104415 (2017).

[44] L. Wang, N. Chepiga, D.-K. Ki, L. Li, F. Li, W. Zhu, Y. Kato, O. S. Ovchinnikova, F. Mila, I. Martin, D. Mandrus, and A. F. Morpurgo, Phys. Rev. Lett. **118**, 257203 (2017).